APPLIED SCIENCES AND ENGINEERING

Multiplexed high-throughput localized electroporation workflow with deep learning–based analysis for cell engineering

Cesar A. Patino[1]†, Nibir Pathak[1,2]†, Prithvijit Mukherjee[1,2]†, So Hyun Park[3], Gang Bao[3], Horacio D. Espinosa[1,2]*

Manipulation of cells for applications such as biomanufacturing and cell-based therapeutics involves introducing biomolecular cargoes into cells. However, successful delivery is a function of multiple experimental factors requiring several rounds of optimization. Here, we present a high-throughput multiwell-format localized electroporation device (LEPD) assisted by deep learning image analysis that enables quick optimization of experimental factors for efficient delivery. We showcase the versatility of the LEPD platform by successfully delivering biomolecules into different types of adherent and suspension cells. We also demonstrate multicargo delivery with tight dosage distribution and precise ratiometric control. Furthermore, we used the platform to achieve functional gene knockdown in human induced pluripotent stem cells and used the deep learning framework to analyze protein expression along with changes in cell morphology. Overall, we present a workflow that enables combinatorial experiments and rapid analysis for the optimization of intracellular delivery protocols required for genetic manipulation.

INTRODUCTION

Recent advances in micro/nanotechnology, molecular biology, and data analysis methods have facilitated the manipulation and analysis of individual cells at high throughput (*1*–*3*). These developments have enabled the precise engineering of cell phenotype for fundamental biological studies and therapeutic applications. Cellular engineering and analysis workflows typically involve the delivery of foreign cargo (e.g., plasmid DNA, Cas9, and RNAs) into cells for the manipulation of their genotype and phenotype. Common methods of delivery include viral particles, chemical carriers, and bulk electroporation, with each method having its own advantages and disadvantages depending on the application of interest (*4*, *5*). For instance, chemical carriers such as Lipofectamine are suitable for adherent cell types but do not perform well for suspension cells, especially those having low endocytic capacity (*6*). Moreover, they may lead to toxicity in certain cell types (*7*). Bulk electroporation provides high delivery and transfection efficiencies for a range of different cell types but can be limited by poor efficiency and viability for sensitive cells such as human induced pluripotent stem cells (hiPSCs) or T cells (*8*, *9*). In addition, recent reports have shown that bulk electroporation can impair downstream gene expression and the functioning of these sensitive cell types (*10*, *11*). Viral methods are often preferred in the case of hard-to-transfect postmitotic cells such as neurons (*12*) and for transfecting pooled vector libraries (RNA interference, CRISPRi, etc.) used in screening studies (*13*) because of their extremely high efficiencies. However, the immunogenic response to viral particles and the random integration of viral DNA in the host genome are remaining concerns (*14*) for use in therapeutics.

Microfluidic methods for intracellular delivery offer a promising alternative to these traditional techniques. The most commonly used microfluidic methods can be broadly categorized as flow-based microfluidic systems, micro- and nanoprobes, and engineered nanosubstrates (*15*, *16*). Flow-based microfluidics such as cell squeezing (*17*), flow-through electroporation (*18*), and other hydrodynamic mechanoporation systems (*19*–*21*) typically pass cells through predefined channel constrictions or flow perturbations that permeabilize the cells, allowing for molecular cargo to enter. These systems are attractive because of their low cost, simplicity of operation, and high throughputs. However, the geometric design of flow-based systems must be adjusted for cells of different sizes and may lead to inconsistent performance in the case of cells with a large size distribution or high aspect ratios (*22*). Because of these factors, flow-based methods provide less control over delivery as compared to some other methods. In addition, some of these systems may suffer from biofouling or clogging issues. On the other hand, micro- and nanoprobe-based methods use micro/nanopipettes (*23*–*26*) or hollow atomic force microscopy tips (such as the nanofountain probe and fluidic force microscopy) (*27*, *28*) for precisely controlled delivery into cells with subcellular resolution. The major drawbacks of these systems are their serial approach that limits throughput. These systems are preferred when an application requires selective delivery within a heterogeneous cell population such as for cell-cell communication studies (*29*). The third category of microfluidic systems, engineered nanosubstrates, uses arrays of high–aspect ratio nanostructures such as nanochannels (*30*–*32*), nanostraws (*33*, *34*), and nanoneedles (*35*, *36*) to either directly penetrate the cell membrane or, in some cases, apply a localized electric field (a process called localized electroporation) to open pores in confined regions of the cell membrane for cargo delivery with minimum cell perturbation. Compared to the other two categories, engineered nanosubstrates provide a balance of the required attributes. For example, they are less sensitive to the molecular cargo and cell type in use and can be operated at moderate to high throughputs (*15*). Moreover, nanosubstrates using localized electroporation have been used for nondestructive temporal analysis

[1]Department of Mechanical Engineering, Northwestern University, Evanston, IL 60208, USA. [2]Theoretical and Applied Mechanics Program, Northwestern University, Evanston, IL 60208, USA. [3]Department of Bioengineering, Rice University, 6500 Main St, Houston, TX 77030, USA.
*Corresponding author. Email: espinosa@northwestern.edu
†These authors contributed equally to this work.

of intracellular contents (*37–40*). As a result, they are appealing tools for in vitro/ex vivo intracellular delivery and cell analysis applications. Nevertheless, because of complex fabrication procedures and poor scalability in some cases, these methods are not yet widely adopted for cellular engineering and analysis.

We have previously demonstrated the microfluidic localized electroporation device (LEPD) that uses track-etched polycarbonate (PC) membranes with nanochannels for intracellular delivery and sampling-based temporal analysis (*31*, *37*, *39*). The major advantage of the LEPD over the other nanosubstrate-based methods is its easy and cost-effective assembly procedure. In addition, the use of optically clear and biocompatible PC membranes enables delivery, long-term culture, imaging, and tracking of cells on chip. This ability to deliver molecules into cells in their native adherent condition is especially desirable for sensitive cell types such as hiPSCs that are prone to dissociation-induced stress and death (*41*). Despite the advantages, the extensive optimization required for hard-to-transfect cells necessitates combinatorial experiments with automated readout that can minimize the consumption of time and resources.

Here, we develop a multiwell plate–format LEPD that enables multiple combinatorial experiments in parallel. We combine the high-throughput LEPD with automated imaging followed by artificial intelligence (AI)–based image segmentation and analysis to rapidly optimize molecular delivery and transfection conditions for a wide range of adherent and suspension cell types. The AI pipeline enables automated quantification of delivery/transfection efficiency and aids in analyzing critical cell morphological features to identify conditions that lead to high delivery efficiency while also preserving cell health and viability. Furthermore, the multiwell plate format facilitates easy integration into biological workflows involving downstream imaging, collection, and processing of cells. Using this system, we were able to attain high transfection efficiency (40 to 85%) for a variety of immortalized cell lines and primary/stem cells while maintaining high cell viability (82 to 95%). We also demonstrate that the LEPD concept is scalable to multiple well plate formats and can be tuned depending on whether the application demands few conditions with higher throughput or optimization of multiple conditions over a wide parametric space. We also show that the LEPD performance is comparable or superior to commercially available carrier-based and bulk electroporation intracellular delivery systems. Last, we demonstrate the potential of the LEPD to achieve functional gene knockdown in hiPSCs and analyze the subsequent changes in protein expression and cellular morphology.

RESULTS

Multiwell plate LEPD design

The ability to apply various electrical pulse conditions in parallel across multiple devices is the central functionality of the multiwell plate LEPD design. In this manner, electroporation protocols can be rapidly and systematically optimized to deliver molecular cargoes of interest into different cell types with a high degree of control. An individual LEPD consists of a glass cell culture well bonded to a PC track-etched membrane where cells, adherent or suspended, are plated and permeabilized upon application of electric pulses (Fig. 1, D and E). The applied electric field is localized at the interface between the cell membrane and the nanochannels, leading to the formation of transient pores in a small area of the cell membrane, which results in a gentle and reversible membrane permeabilization mechanism (*32*, *37*). To apply the electrical stimulation, the LEPD is placed between two electrodes: a bottom electrode interfacing with the delivery cargo underneath the PC membrane and a top electrode that is immersed in the electroporation buffer (EP buffer). To parallelize this setup, a printed circuit board (PCB) patterned with gold-plated pads is aligned and bonded to a bottomless multiwell plate (Fig. 1, A to C), which together comprise the bottom electrode assembly. Similarly, the top electrode assembly consists of a PCB that contains a pattern of plated through-holes where gold-plated electrodes are inserted

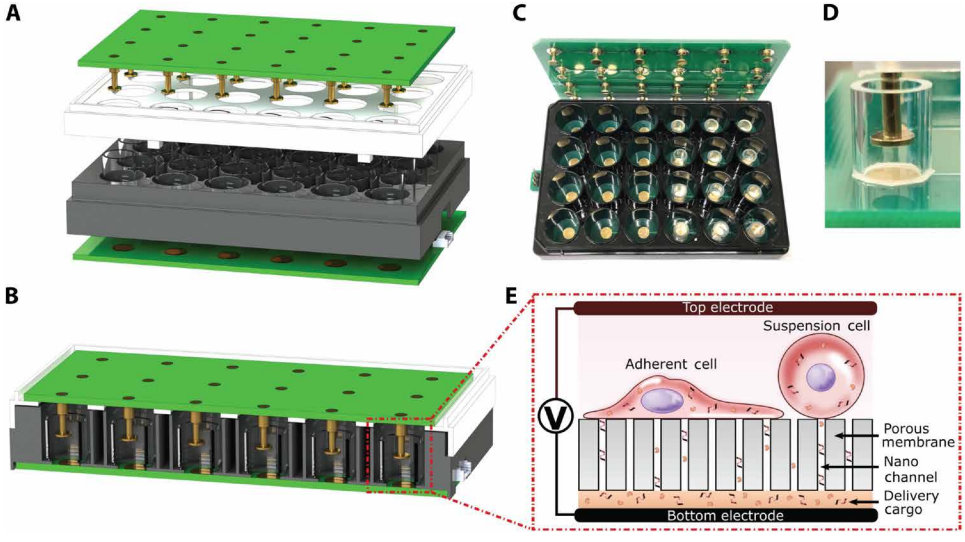

Fig. 1. Concept schematic. (**A**) Exploded-view computer-aided design (CAD) diagram of the multiwell LEPD design consisting of the following components from top to bottom: PCB board with push-fit electrodes, spacer plate, LEPDs, bottomless well plate, and PCB board with electrode pads. (**B**) Cross-sectional view of the assembled LEPD system. (**C**) Photograph of the assembled 24-well LEPD system. LEPDs inserted in the right half of the multiwell plate. (**D**) Photograph of an individual LEPD placed between the bottom pad electrode and the top stub electrode. (**E**) Conceptual illustration of localized electroporation–induced delivery into adherent or suspended cells using LEPD.

using push-fit receptacles. To complete the assembly before electroporation, 4-μl droplets of the delivery reagent followed by the LEPDs are placed on top of the bottom electrode pads, then the top electrode assembly, which fits tightly on top of the multiwell plate, is placed to ensure precise alignment and facile assembly. The top and bottom PCBs are connected to a function generator that can be programmed to apply electric pulses of various shapes (e.g., square, bilevel, and exponential), voltage amplitudes, pulse durations, pulse numbers, and frequencies. Each row of the multiwell LEPD array can be independently addressed, which enables the application of multiple pulse conditions across devices in one experiment. For example, one optimization protocol may involve the application of multiple voltage conditions across rows to deliver molecular cargoes with varying concentrations across the columns. The multiwell LEPD platform facilitates and expedites the optimization of molecular delivery protocols, which is a necessary step to achieve the desired performance (e.g., efficiency and viability) for a given cell engineering application. Moreover, the LEPDs with the biocompatible and transparent substrates facilitate long-term cell culture and imaging, which makes the multiwell LEPD system ideally suited for medium- to high-throughput experiments and subsequent data acquisition. Therefore, once a particular delivery protocol is optimized, the multiwell LEPD can be used to process hundreds of thousands of cells at a time, which substantially increases the throughput of substrate-based electroporation platforms.

Automated image analysis workflow

To extract morphology and intensity information from individual cells in each LEPD following the multiwell delivery experiments, we developed an automated imaging and analysis workflow. The workflow (Fig. 2A) involves transferring the LEPDs to a transparent well plate after electroporation, imaging each well using a microscope equipped with a motorized stage, segmenting the cells in each image using an AI detection pipeline, and extracting shape and intensity features from each cell for analysis using statistical tools. A fully convolutional network (FCN) architecture (*42*) was implemented and trained to segment individual cells or nuclei in fluorescent or phase-contrast micrographs. The FCN contains 20 hidden layers arranged in an encoder-decoder scheme (*43*, *44*) (Fig. 2B) that outputs a multiclass probability used to classify each pixel in the image into three classes (interior, boundary, or exterior). Once the cell or nuclei objects are identified in each image, they are passed through a feature extraction pipeline [CellProfiler (*45*)] that can measure various intensity, shape, texture, and environment features (see examples in table S1). Each feature was transformed using the generalized log (glog) method (*46*) and normalized using robust *z* score (*R.Z.* score) standardization to enable comparison of features using the same scale. To reduce the number of features and improve the interpretability of the data, a feature selection method was used in which highly correlated features were iteratively removed (*47*). Furthermore, a dimension reduction method, uniform manifold approximation and projection (UMAP) (*48*), was used to visualize the high-dimensional data on a corresponding two-dimensional (2D) projection. This workflow was used to calculate performance metrics such as delivery/transfection efficiency and viability, in addition to other metrics related to cell morphology (e.g., area, circularity, and eccentricity), and analyze their relationships. As a result, the automated image analysis pipeline enabled the correlation of experimental inputs to the phenotypic outputs across devices in the multiwell LEPD.

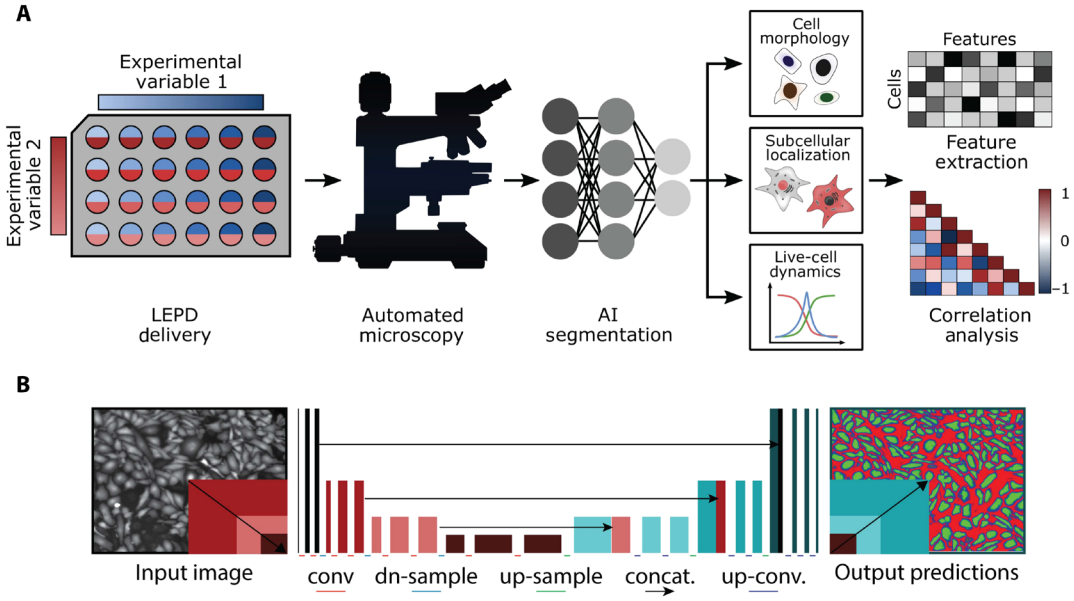

Fig. 2. Image analysis workflow. (**A**) Experimental and analysis workflow of the multiwell LEPD system consists of the following steps (from left to right): combinatorial delivery experiments, automated imaging of each well, cell and nuclei identification using deep learning algorithms, extraction of cellular features (morphology, subcellular localization, and dynamics), and feature postprocessing and correlation analysis. (**B**) Architecture of FCN used to segment the cells and nuclei in an image. Input image is passed through 20 hidden layers consisting of convolution, downsampling, upsampling, concatenation, and up-convolution operations that result in a three-class (exterior, interior, and border) probability map for each pixel in the image. Layers are color-coded on the basis of changes in dimensions (height and width) down and up the encoder and decoder portions of the network, respectively. The thickness of each layer line is proportional to the width of the layer. For a 520 × 696 grayscale image, there are 7,787,523 trainable parameters in the network.

Device architecture optimization

The performance of the LEPD system is dictated by the design of the system and the experimental inputs. However, to obtain meaningful outputs from the experimental inputs, the uniformity of electroporation within devices and between the rows and columns of the multiwell array must be characterized and optimized to minimize variability.

To characterize the intradevice cell-to-cell electroporation variability, we stained cells with calcein AM and applied a series of electric pulses to permeate the cells and extract the intracellular fluorescent calcein from the cells while imaging the process in real time. An indium tin oxide substrate was substituted in place of the bottom PCB for these experiments to enable real-time imaging. The fluorescent calcein was depleted from electroporated cells in both adherent (HeLa; Fig. 3A) and suspended cells (K562; fig. S1A), as shown in the series of micrographs acquired during the application of the pulses. The dynamics of this process (Fig. 3B and fig. S1B) reveal cell-to-cell variability in total calcein depletion and rate of depletion for both adherent and suspended cells. The rate of depletion time constant, τ, was calculated by fitting an exponential function to the temporal normalized intensity loss data. Furthermore, a photobleaching correction factor was calculated from control experiments where cells were unperturbed and imaged to improve the fitting and correct for photobleaching. To investigate whether the morphology

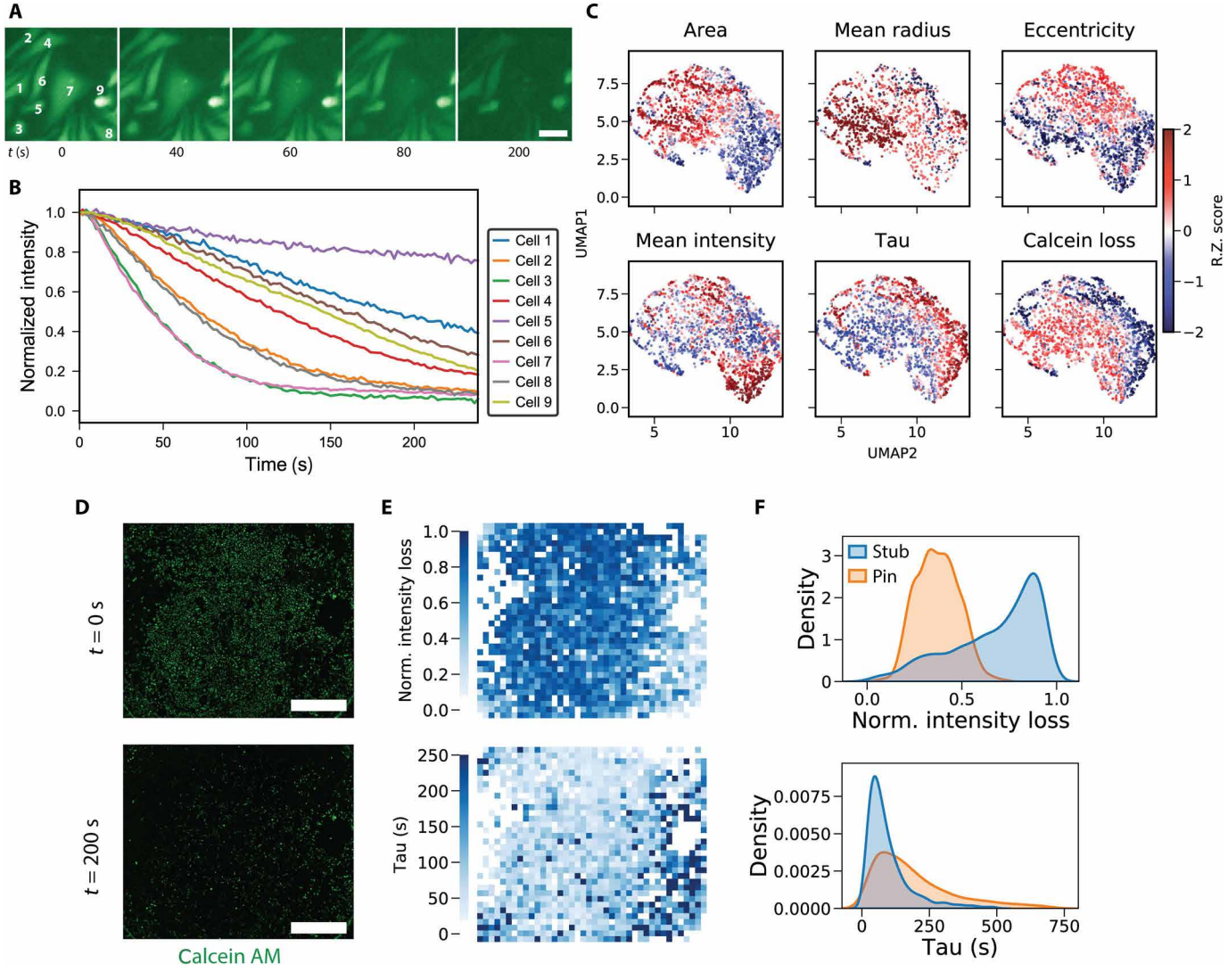

Fig. 3. System characterization and optimization. (**A**) Fluorescence micrographs of calcein AM–stained HeLa cells acquired during electroporation. Horizontal axis labels the indicated time (seconds). Images shown represent a subset region (50 × 50 pixels) of the acquired micrograph (2560 × 2160 pixels) with cells numbered in the first image ($n_{cells} = 9$). Scale bar, 20 μm. (**B**) Line plot of fluorescence intensity normalized by the initial intensity versus time of each cell numbered in (A). (**C**) UMAP projections of high-dimensional calcein sampling dataset containing intensity ($t = 0$ s), shape ($t = 0$ s), and experimental measurements ($t = 0$ to 200 s) from each cell ($n_{cell} = 4390$). All features were standardized using the *R.Z.* score method as illustrated by the color map of selected features. (**D**) Fluorescence micrograph (2560 × 2160 pixels) of the calcein AM–stained cells plated in an LEPD before ($t = 0$ s) and after electroporation ($t = 200$ s). Scale bars, 1 mm. (**E**) Spatial heatmaps of the normalized intensity loss and time constant (τ), calculated from the exponential function $I = I_0 (1 - c) \times e^{-t/\tau} + c$ of cells in (D). (**F**) Kernel density plots of the distribution of normalized intensity loss and τ for two top electrode geometries: straight pin and nail-head stub.

of the cells plays a factor in the intradevice electroporation variability, the AI imaging and analysis pipeline was used to identify the cells in the images and extract their corresponding shape features. A Pearson correlation heatmap in fig. S2 reveals highly correlated shape and intensity features that were iteratively removed to simplify the analysis. The remaining features were projected on a 2D scatterplot (see Fig. 3C) using the UMAP dimension reduction technique. The divergent color map of each UMAP scatterplot was used to illustrate the standardized *R.Z.* score of selected shape features in addition to the experimental outputs τ and normalized calcein loss for visual comparison. Upon inspection, it is evident that cells with higher depletion magnitude and faster depletion rates tend to be larger and more spread out (e.g., area and eccentricity). Conversely, circular cells with higher initial intensities do not deplete as much or as fast. Cells that are more spread out are likely better adhered on the substrate as compared to cells with more rounded morphology. Therefore, the degree of adhesion possibly affects membrane permeabilization, which is consistent with theoretical electroporation models and experimental reports (*37*). Viability was measured to be around 90.89% 24 hours after electroporation using propidium iodide (PI) assay, which indicates that the calcein depletion in about 90% of the cells was due to reversible permeabilization. In the case of suspended cells, in which the cells are centrifuged before electroporation, the dynamics of calcein depletion are more sporadic (fig. S1, A and B). The mean fluorescence intensity (MFI) obtained after electroporation correlates with the SD of intensity from phase-contrast micrographs obtained for the same field of view (fig. S1, C and D). We hypothesize that the cells with lower intensity variability in phase contrast are flatter and therefore in better contact with the nanochannel substrate, which may result in higher calcein extraction (i.e., lower final fluorescence intensity).

Next, we examined the effects of the top electrode geometry on the intradevice spatial variability of calcein depletion within LEPDs by using two different top electrode geometries: straight pin and nail-head pin (stub). Micrographs obtained at the beginning and end of the pulse application reveal that calcein was depleted for both the stub (Fig. 3D) and pin geometries compared to a control device where no pulses were applied (fig. S3, B and C). Spatial heatmaps (Fig. 3E and fig. S3D) were used to visualize the spatial variability of τ and normalized intensity loss due to calcein depletion for the stub electrode, pin electrode, and control LEPDs. The stub geometry resulted in a more spatially uniform calcein depletion throughout the device compared to the pin as observed from the spatial heatmaps. Moreover, the amount and rate of calcein loss were also greater for the case of the stub as seen from the kernel density distribution plots (Fig. 3F) and bar plots (fig. S3, E and F). The calcein depletion from the control device caused by photobleaching was significantly less ($P < 0.00001$) than that of electroporated LEPDs (fig. S3E). We hypothesized that the spatial variation in the electric field produced by the two electrode geometries resulted in the difference in uniformity of calcein depletion observed in our experiments. To that end, we determined the spatial locations of the pin and stub electrodes before the experiments using phase-contrast imaging (fig. S3A) and mapped to the corresponding fluorescent micrographs and heatmaps (fig. S3, B to D). The resulting images show that for the pin electrode, higher calcein depletion occurred near the electrode center compared to regions away from the center, while we observed a more uniform depletion over a greater area for the electrode with the stub geometry. These results affirm the hypothesis that the electric field distribution in the LEPD is a function of the electrode geometry. To further study the electric field distribution within an LEPD with both top electrode geometries, we carried out a multiphysics simulation (fig. S4), which modeled a single LEPD containing the electrodes, a layer of cells, and delivery cargo. Results from the multiphysics simulations of the two geometries reveal that the localized transmembrane potential is higher for the stub geometry compared to the pin geometry (fig. S5) for the same applied voltage, which is consistent with the higher depletion observed with the stub geometry in the experiments. Moreover, the change in transmembrane voltage along the radial direction is slightly more pronounced for the pin geometry, which could lead to spatial nonuniformities as observed in the experiments. In lieu of the experimental and simulation results, the stub geometry was used for all subsequent electroporation experiments.

For assessing interdevice variability across the multiwell plate for intracellular delivery, a fluorescently labeled DNA oligonucleotide was delivered into HeLa cells in 12 LEPDs (fig. S6A) arranged in a 3 × 4 array within the LEPD well plate system using the same electroporation pulse conditions (V = 20 V, frequency = 10 Hz, N_{pulses} = 400). Following electroporation, the cells in all devices were stained with Hoechst dye to demarcate the locations of the nuclei and to calculate the delivery efficiency of the DNA oligonucleotide. The oligonucleotide was delivered in all devices with efficiencies above 90%. To visualize spatial effects across the plate, the standardized mean intensity and signal-to-noise ratio (SNR) were obtained for each LEPD in the multiwell plate (fig. S6B). To calculate the statistical variability across rows and columns, a two-way analysis of variance (ANOVA) test was implemented (fig. S6C). The ANOVA results show that there is no significant variability in the SNR across the rows and columns and the combination of the two ($P > 0.05$; fig. S6). The uniformity of delivery across the multiwell LEPD is an essential performance criterion for high-throughput experiments to draw meaningful conclusions from the experimental inputs. Furthermore, to characterize the scalability of the LEPDs for functional biomolecular delivery, a green fluorescent protein (GFP)–encoding plasmid was delivered in LEPD wells of various sizes ranging from 2 to 6 mm in diameter. Fluorescent micrographs obtained 24 hours after electroporation (fig. S7) show successful delivery for all LEPD well sizes. The scalability of the multiwell LEPD provides flexibility when it comes to tailoring the experimental design for either optimization (e.g., more conditions with smaller devices) or high-throughput (e.g., less conditions with larger devices) applications.

Electroporation optimization

In addition to the device architecture, the efficiency of the LEPD, similar to any electroporation system, depends on many experimental factors ranging from different pulse parameters to buffer types and concentration of delivery cargo. For any specific application, it is desirable to optimize the various experimental conditions. The multiplexed format of the current system allows for quick optimization by varying two experimental factors over their respective ranges along both the axes of the well plate. We first show the variation of the transfection efficiency of a *GFP* plasmid delivered into human embryonic kidney (HEK) 293T cells for a range of pulse voltages under two different buffer conditions (Fig. 4A). Along one axis, we varied the voltage from 10 to 40 V, while the buffer condition was varied along the other with three samples per condition. The transfection efficiency increases from 10 to 20 V and sharply

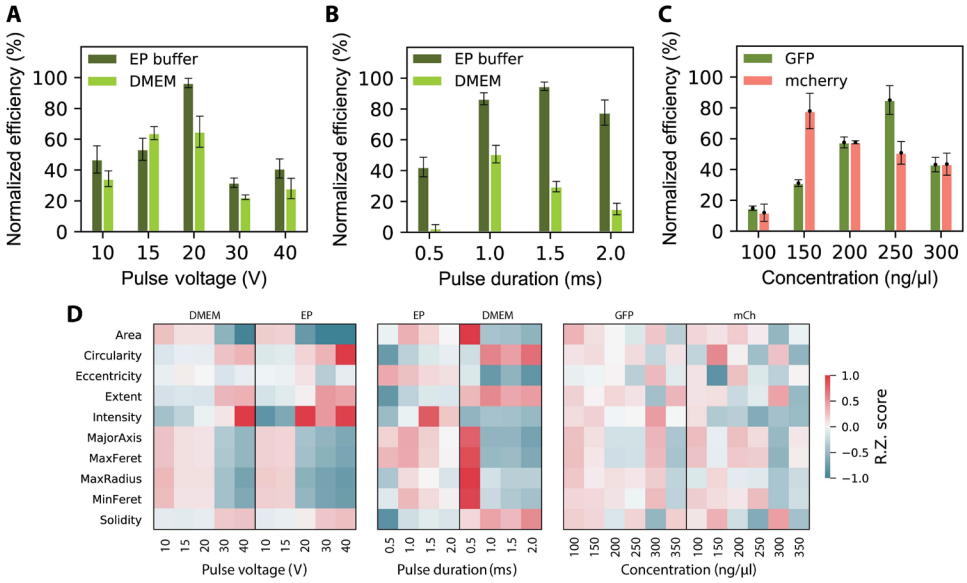

Fig. 4. Optimization of electroporation conditions. (**A**) Variation of transfection efficiency with pulse voltage for HEK 293T cells electroporated in cell culture media (DMEM) and EP buffer using LEPD. (**B**) Variation of transfection efficiency with pulse duration for HEK 293T cells electroporated in DMEM and EP buffer using LEPD. (**C**) Variation of transfection efficiency with plasmid concentration for HEK 293T cells transfected with pmax GFP– and mCherry-encoding plasmids using LEPD. All error bars indicate the SEM of triplicate samples, $n_{cell} > 100$ per sample for all bar plots. All transfection efficiencies are normalized with respect to the highest value of efficiency in each plot. The highest efficiencies for plots in (A) to (C) are 71.6, 63.6, and 47.7%, respectively. (**D**) Heatmap of standardized (*R.Z.* score) extracted features (vertical axis) from experimental inputs (horizontal axis).

decreases thereafter for both the EP buffer and cell culture medium [Dulbecco's modified Eagle's medium (DMEM)]. Furthermore, the viability (fig. S8) is high from 10 to 20 V and decreases at 30 and 40 V for both EP buffer and DMEM. From the data, it was clear that a voltage of 20 V with the cells incubated in the EP buffer resulted in the maximum transfection efficiency. Similarly, we also evaluated the effect of pulse duration under both buffer conditions (Fig. 4B). A pulse duration of 1.5 ms worked best when used with cells incubated in the EP buffer during pulsing. Overall, the performance with respect to transfection efficiency is better with the cells incubated in the EP buffer during pulse application as compared to having them in cell culture medium (DMEM). It is also known that delivery or transfection efficiency depends on the concentration of the delivery cargo. Therefore, we also evaluated the dependence of concentration on transfection efficiency for two different plasmids encoding for fluorescent reporter protein expression (GFP and mCherry) (Fig. 4C). As evident from the data, there exists an optimal concentration for both the plasmids, which is 250 ng/µl for the *GFP* and 150 ng/µl for the *mCherry* plasmid. The existence of an intermediate optimal concentration is expected as too low a concentration means fewer molecules available for delivery, while too high a concentration can lead to DNA toxicity in cells. Consistent with this hypothesis, we observed a reduction in the viability from 92.30 to 79.85% between the 100 and 300 ng/µl concentrations, respectively.

In addition, we also analyzed cell morphology features for all conditions (24 hours after transfection) to determine whether the experimental inputs result in visible changes in cell shape. A heatmap of several shape features and the corresponding experimental inputs (Fig. 4D) illustrates these effects. Evidently, increasing the voltage amplitude and pulse duration results in the rounding of cells and reduction in the average cell area as compared to control cells. These effects are more amplified for the conditions using DMEM as compared to EP buffer. Similar results are observed by increasing the plasmid concentration, although to a lesser extent. These results indicate that pulse strength, buffer, and plasmid concentration can lead to alterations in the cell morphology compared to unperturbed cells, which may be the result of the cells' response to the electric field or DNA toxicity effects. Since drastic morphological changes may be accompanied by undesirable downstream effects in the cells, the electroporation conditions that result in high efficiency while maintaining morphology close to that of control cells are desirable for most applications. Overall, this framework of optimization experiments and the subsequent AI-assisted image analysis demonstrates how the multiplexed format of the 24-well plate LEPD allows for quick optimization of the multiple experimental factors required for efficient intracellular delivery while keeping undue electroporation-induced morphological changes to a minimum.

Cell-agnostic versatile cargo delivery

Intracellular delivery of functional molecular cargo is an essential step in fundamental biological research and in clinical applications. The type of molecular cargo used could range from various kinds of nucleic acids such as plasmid DNA, oligonucleotides, and small interfering RNA (siRNA) to protein complexes such as Cas9 ribonucleoproteins (RNPs). After optimizing the device architecture and electroporation protocols, we tested the performance of the LEPD system for intracellular delivery in a range of different cell types. For arriving at the optimal electroporation conditions (pulse voltage, duration, plasmid concentration, etc.) for molecular cargo delivery into a cell type, we followed the optimization workflow presented in the previous section. Furthermore, we compared efficiencies of transfection and viability to two well-established techniques, lipid-vesicle carriers and bulk electroporation, which are commercially available.

To evaluate the delivery efficiency of the multiwell LEPD, we first delivered a fluorescently labeled DNA oligonucleotide in both adherent and suspended cell lines as well as in hard-to-transfect human primary and stem cells (fig. S9). Oligonucleotides are known to specifically bind to intracellular target molecules and have been used for targeted therapy by processes such as selective mRNA degradation and blocking of transcription factors (*49–51*). We found that the efficiencies of oligonucleotide delivery with the LEPD ranged from 78% to more than 90% for all the investigated cell types (fig. S9G).

Plasmid DNA is one of the most widely used nonviral vectors for introducing functional genetic modifications in cells. For instance, plasmids that encode Cas9 have been used in the CRISPR system aimed toward reprogramming of T cells for enhanced cytotoxicity against PD-L1–expressing tumor cells (*52*). Plasmid DNAs carrying Cas9, guide RNA (gRNA), and donor templates have also been used to introduce point mutations in patient-derived iPSCs (*53*). In comparison to RNA and viral vectors, plasmids are also easier and cheaper to produce and have a longer shelf life. Therefore, to evaluate the introduction of large functional biomolecules into different cell types using the LEPD, we first delivered a plasmid (*pmax GFP*) into two adherent cell lines [HeLa (Fig. 5A) and HEK 293T (fig. S10)]. The transfection efficiency was 83.04 and 76.76% for HeLa and HEK 293T cells, respectively (Fig. 5E). Furthermore, the transfection efficiency achieved for HeLa was significantly higher ($P < 0.05$) than that obtained using Lipofectamine 3000 (LIPO), while it was comparable to LIPO for the case of HEK 293T. Then, we attempted plasmid delivery into a model-suspended cell line (K562; Fig. 5B). The transfection efficiency (63.10%) for the K562 cells was significantly higher ($P < 0.001$) using the LEPD than that obtained with LIPO-mediated transfection (22.63%) (Fig. 5E). The relatively lower delivery/transfection efficiency (Fig. 5E and fig. S9G) of the K562 cells is possibly due to them being nonadherent to the porous membrane substrate as opposed to adherent cells such as HeLa and HEK 293T. This reinforces the observation made in the preceding section where cells with a larger area and possibly stronger adhesion to the substrate lost relatively more calcein due to LEPD-mediated electroporation.

Next, we performed plasmid delivery in adherent/suspended hard-to-transfect and sensitive cell types such as primary human dermal fibroblasts (HDFs), hiPSCs, and sickle human umbilical cord–derived erythroid progenitors (S-HUDEP2), which is an immortalized $CD34^+$ hematopoietic stem cell–derived erythroid progenitor cell line carrying biallelic sickle mutations in *beta-globin* gene (Fig. 5, C and D, and fig. S10) (*54*). These cell types have a range of applications such as disease modeling, cell-based therapies, and developmental or regeneration studies (*55–57*). We compared the transfection efficiency of the LEPD for these cell types to that of a commercially available bulk electroporation system. The transfection efficiencies obtained for the LEPD-treated HDFs (73.19%) and hiPSCs (43.03%) were significantly higher ($P < 0.05$) than those obtained in the case of bulk electroporation. There was no significant difference in transfection efficiencies between the two methods in the case of the S-HUDEP2 cells (Fig. 5G). As expected, the transfection efficiencies for the hard-to-transfect cell types were lower compared to those of the cell lines investigated earlier.

In addition to transfection efficiency, we also evaluated the viability of all the cell types 24 hours after treatment with the LEPD (fig. S11). Among the continuous cell lines, the viability for the LEPD-treated cells ranged from 90 to 96% (Fig. 5F and fig. S11), while for the hard-to-transfect cell types, the viability was around 85 to 90%. The viabilities observed for the hard-to-transfect cells were significantly higher ($P < 0.05$) than those obtained for the same cells treated with bulk electroporation, especially for S-HUDEP2, where the viability in the case of bulk electroporation was 49.14% compared to 89.52% in the case of LEPD-treated cells (Fig. 5H and fig. S11).

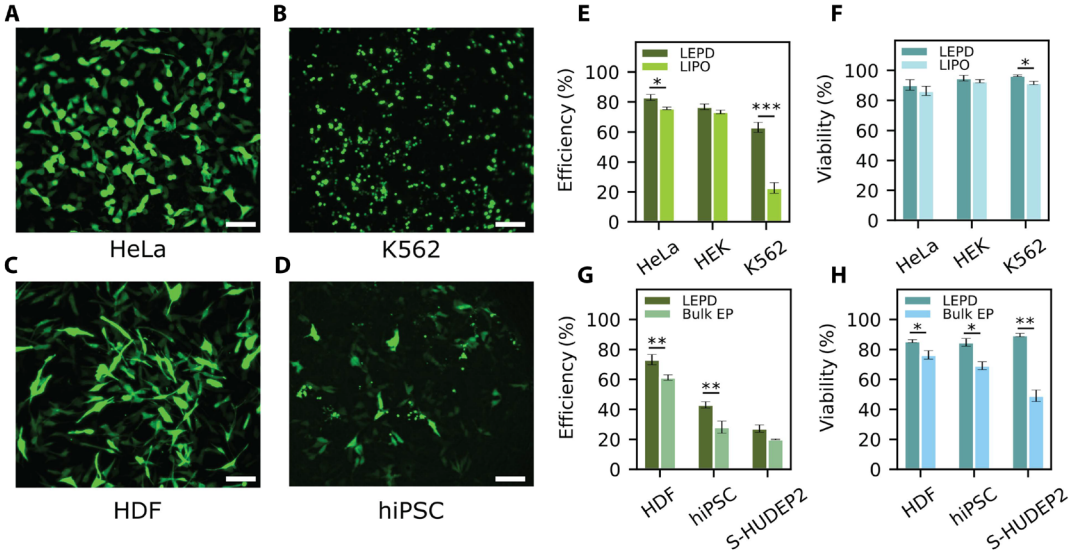

Fig. 5. Cell-agnostic versatile cargo delivery. (**A** to **D**) Representative images of successful transfection of fluorescent protein–encoding plasmids into HeLa (adherent), K562 (cells in suspension), primary HDFs, and human hiPSCs. hiPSCs were delivered with an mCherry-encoding plasmid, while the other cells were transfected with a pmax GFP–encoding plasmid. hiPSCs are pseudo-colored green. (**E**) Plasmid transfection efficiency of LEPD and LIPO for various continuous cell lines 24 hours after delivery. (**F**) Viability of various continuous cell lines 24 hours after treatment with LEPD and LIPO. Error bars indicate SEM. (**G**) Plasmid transfection efficiency of LEPD and bulk electroporation (bulk EP) for various hard-to-transfect cell types 24 hours after delivery. (**H**) Viability of various hard-to-transfect cell types 24 hours after treatment with LEPD and bulk electroporation (bulk EP). All error bars indicate the SEM of triplicate samples, $n_{cell} > 100$ per sample for all bar plots. *$P < 0.05$, **$P < 0.01$, and ***$P < 0.001$. Scale bars, 100 μm.

Moreover, we also observed that in the bulk electroporation protocol, there is a significant loss of cells. For instance, in the case of HDFs, we counted the number of adhered live cells 24 hours after electroporation for bulk-electroporated and LEPD-treated samples. We compared the cell numbers for each condition to their respective control samples, which were seeded at the same density as the processed cells. We found that in the case of bulk electroporation, the samples had 60% fewer cells ($P < 0.001$) as compared to the control (fig. S12). We did not observe any such cell loss in the LEPD samples when compared to nonelectroporated controls. This cell loss in bulk electroporation can be attributed to cell death owing to the high electric fields experienced by the cells in the bulk electroporation system. This observation suggests that the LEPD may provide an advantage over bulk electroporation in clinical studies where patient-derived cells are used, which could be rare, hard to obtain, and cannot be propagated indefinitely. Overall, our results indicate that the LEPD can be used for delivering small biomolecules such as oligonucleotides to large biomolecular cargo such as plasmids into a variety of cell types while preserving cell viability.

Delivery precision and controlled multicargo delivery

In addition to cell-agnostic cargo delivery, precise control over the cargo amount delivered is also essential in many biological protocols for applications ranging from gene editing to cellular reprogramming (*58*, *59*). Here, we investigated the precise control over plasmid transfection–mediated protein expression enabled by the LEPD system and compared its performance to that of LIPO. A plasmid encoding for the expression of GFP was delivered using both the LEPD and LIPO into HeLa and K562 cells. A comparison of the two transfection methods based on the distributions of the normalized fluorescence intensities of the expressed GFP in both HeLa and K562 cells is shown in Fig. 6 (A and B, respectively). The variance of

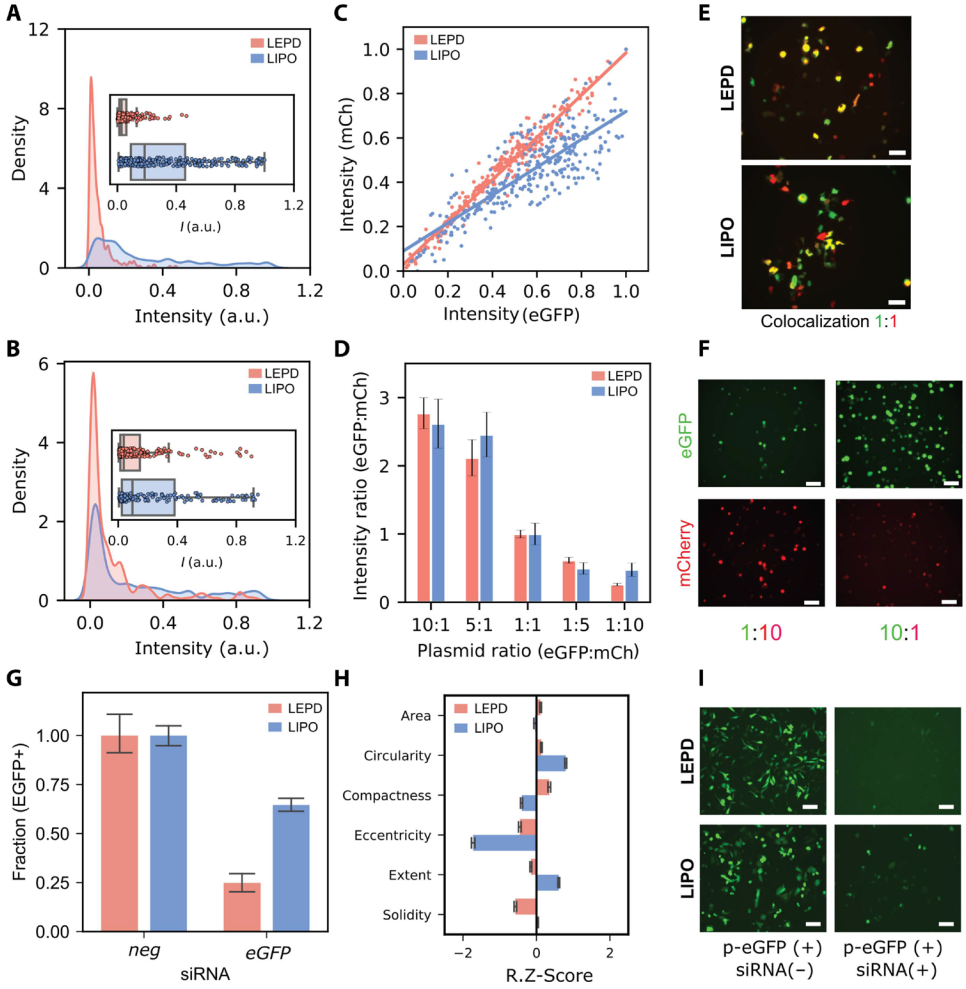

Fig. 6. Delivery precision and controlled multicargo delivery. (**A** and **B**) Distribution of normalized fluorescence intensities of GFP-expressing HeLa (A) and K562 (B) cells 24 hours after *GFP* plasmid transfection, LEPD (red), and LIPO (blue) ($n_{cell} > 200$ per condition). (**C**) Scatterplot: Normalized log fluorescence intensities of mCherry (mCh) and eGFP in HEK 293T cells cotransfected with a 1:1 concentration ratio of *mCh* and *eGFP* plasmids ($n_{cell} > 200$ per condition), data fitted to $y = mx + c$. $R^2_{LEPD} = 0.96$, $R^2_{LIPO} = 0.68$, $m_{LEPD} = 0.95$, $m_{LIPO} = 0.63$. (**D**) Intensity ratio (eGFP:mCh) in HEK 293T cells cotransfected with plasmid mixtures of different concentration ratios. $n_{cell} > 50$, error bars represent SEM for triplicate samples. (**E**) Representative images of the 1:1 case from (D). Scale bars, 20 μm. (**F**) Representative images of the 1:10 and 10:1 LEPD cases from (D). Scale bars, 100 μm. (**G**) siRNA knockdown of eGFP in HeLa cells transfected with *eGFP* plasmid. Fraction of eGFP-expressing cells was obtained by normalizing with respect to negative (neg) control. (**H**) Morphology features relative to control unperturbed cells. Features were standardized using *R.Z.* score. (**I**) Representative fluorescent micrographs of plasmid and siRNA codelivery using LEPD and LIPO, respectively. Scale bars, 50 μm. a.u., arbitrary units.

the normalized intensity of GFP in LIPO-transfected cells was significantly higher (Levene's test, $P < 10^{-5}$) than that of the cells transfected via the LEPD. Similarly, data corresponding to the distribution of fluorescence intensity for other cell types transfected using LEPD and LIPO/bulk electroporation are shown in fig. S13. Next, we codelivered two plasmids expressing fluorescent reporter proteins, eGFP and mCherry, respectively, into HEK 293T cells using both the LEPD and LIPO. The plasmid mixture used for delivery had both the plasmids in equal concentration (1:1 concentration ratio, 200 ng/μl per plasmid type). Plasmid codelivery using both the transfection methods resulted in cells simultaneously expressing both proteins (Fig. 6E). To get an estimate of the control and precision of codelivery of plasmids in equal concentration, we plotted the normalized fluorescent intensities of ~600 cells from both the green (GFP) and the red channel (mCherry) (Fig. 6C). Fitting of the normalized fluorescence intensity data to a linear model ($y = mx + c$) suggests that the ratio of mCherry to GFP expression is closer to the desired value of 1:1 for cells transfected with the LEPD system (red line, slope = 0.95) as compared to the cells treated with LIPO (blue line, slope = 0.63). Moreover, the expression ratio of mCherry to GFP has a tighter distribution for the LEPD-treated cells ($R^2 = 0.96$) as compared to those treated with LIPO ($R^2 = 0.68$) (Fig. 6C). In addition, we also demonstrated the ability to control the relative expression levels of the two reporter proteins by varying the relative concentrations of their plasmid vectors in the delivery buffer (Fig. 6, D and F). These results demonstrate that the LEPD enables multicargo delivery with precise control over the dosage.

Next, we tested the multiwell LEPD system for optimization of siRNA knockdown by codelivering an eGFP-expressing plasmid together with either a siRNA containing the *eGFP* sequence or a siRNA with a scrambled sequence as a negative control. We delivered increasing concentrations of siRNA ranging from 250 to 2000 nM and observed substantial knockdown (>70%) of eGFP-expressing cells for all concentrations after 24 hours of delivery (fig. S14). Next, we compared the performance of LEPD to LIPO using a 500 nM concentration of siRNA and observed enhanced knockdown in the case of LEPD compared to LIPO (Fig. 6, G and I). Furthermore, we examined the morphological features of the cells after the treatment using the AI image analysis pipeline and compared the standardized features relative to unperturbed cells (Fig. 6H). These results suggest that the cells transfected using the LEPD were phenotypically closer to the controls compared to cells transfected using LIPO.

The ability to deliver multiple cargoes with precise dosage control can be useful in applications such as CRISPR-Cas9 system–mediated gene editing, wherein it has been shown that the genome modification efficiency and percentage of off-target effects can highly depend on the corresponding RNP or gRNA concentration (*60*, *61*). Multiple cargo delivery can also be useful in combinatorial siRNA- or CRISPR-based multigene knockdown studies for the identification of signaling pathway interactions and gene regulatory networks (*62*, *63*). In addition to gene editing applications, the precision in intracellular delivery can also be important in studies involving the induction of hiPSCs, wherein efficient induction is shown to depend on the relative concentration of reprogramming factors that are introduced (*58*, *64*). Thus, the multiwell LEPD system coupled with the AI-enabled automated imaging and analysis pipeline can facilitate the optimization of high-throughput cell perturbation protocols without disrupting cell phenotype, which is essential to prevent unwanted downstream effects that are not accounted for in the design of the experiment.

Functional gene knockdown in hiPSCs

The efficient delivery of genetic perturbation agents, such as siRNA molecules or CRISPR-Cas9 complexes, into clinically relevant cell types provides a framework for studying gene function, developmental pathways, effects of drugs, and disease mechanisms. In the example of stem cell therapy, somatic cells obtained from patients can be generated into pluripotent stem cells (*65*), differentiated into a cell type of interest, and reintroduced into the patient to target a disease (*66*). Therefore, understanding the factors that affect pluripotency is necessary to achieve the desired therapeutic outcome. To demonstrate the utility of the multiwell LEPD system in this context, we delivered siRNA targeting the pluripotency marker Oct4 (also known as *POU5F1*) into hiPSCs and subsequently performed immunostaining to analyze the consequent changes in Oct4 protein expression. Oct4 has been previously reported to interact and regulate levels of β-catenin, which are important for maintaining pluripotency and self-renewal (*67*). Fluorescent micrographs of the hiPSCs (see Fig. 7A) captured after immunostaining with Oct4- and β-catenin–specific antibodies 72 hours after siRNA delivery revealed a significant reduction in Oct4 protein levels in cells electroporated with the *Oct4* siRNA compared to cells electroporated with a scrambled-sequence siRNA (negative control). Furthermore, the β-catenin fluorescence signal is present in both the control cells and the Oct4 knocked-down cells. Upon closer inspection of selected regions of interest (Fig. 7B), we observed differences in the intensity gradients of β-catenin across the cells. We measured the fluorescence intensity of β-catenin and 4′,6-diamidino-2-phenylindole (DAPI) for a few cells (Fig. 7C) along line segments to determine the intracellular localization of β-catenin. Evidently, β-catenin is expressed in higher concentrations at the membrane of *Oct4* siRNA–treated cells, whereas the concentration of β-catenin is more uniform for the control cells.

To quantify the results of the Oct4/β-catenin immunostaining for all the cells in the devices, we used the deep learning segmentation workflow to identify each cell and used the feature extraction pipeline to obtain hundreds of intensity and shape measurements for each cell. As a result, we could generate distribution profiles for each measurement of interest (Fig. 7D) to compare the two conditions. The distribution profile of the MFI of nuclear Oct4 reveals that the vast majority of cells treated with the *Oct4* siRNA have lower Oct4 expression than the controls. Specifically, 92.5% of cells treated with *Oct4* siRNA had lower nuclear Oct4 MFI than the lower 10th percentile of the control cells. The nuclear MFI distribution of β-catenin is not as distinct between the two conditions, but the *Oct4* siRNA–treated cells have a relatively larger spread than the controls. Conversely, the membrane MFI of β-catenin is higher for the *Oct4* siRNA–treated cells for most of the cells as we had observed from the representative line scans from Fig. 7C. Moreover, the SD of intensity measured for the entire cell is higher for the *Oct4* siRNA–treated cells, which is consistent with our observation that the intensity gradients in the Oct4 knocked-down cells are more pronounced than those in the controls. We obtained aggregate statistics for each device to assess statistical significance in the expression levels of Oct4 and β-catenin for the two siRNA treatments. There is a statistically significant decrease ($P < 0.01$) in Oct4 expression in the *Oct4* siRNA–treated cells relative to the controls (Fig. 7E), which shows that the LEPD-mediated siRNA delivery resulted in the efficient knockdown of Oct4 in hiPSCs. Furthermore, we calculated the total fluorescence intensity of β-catenin in the entirety of each

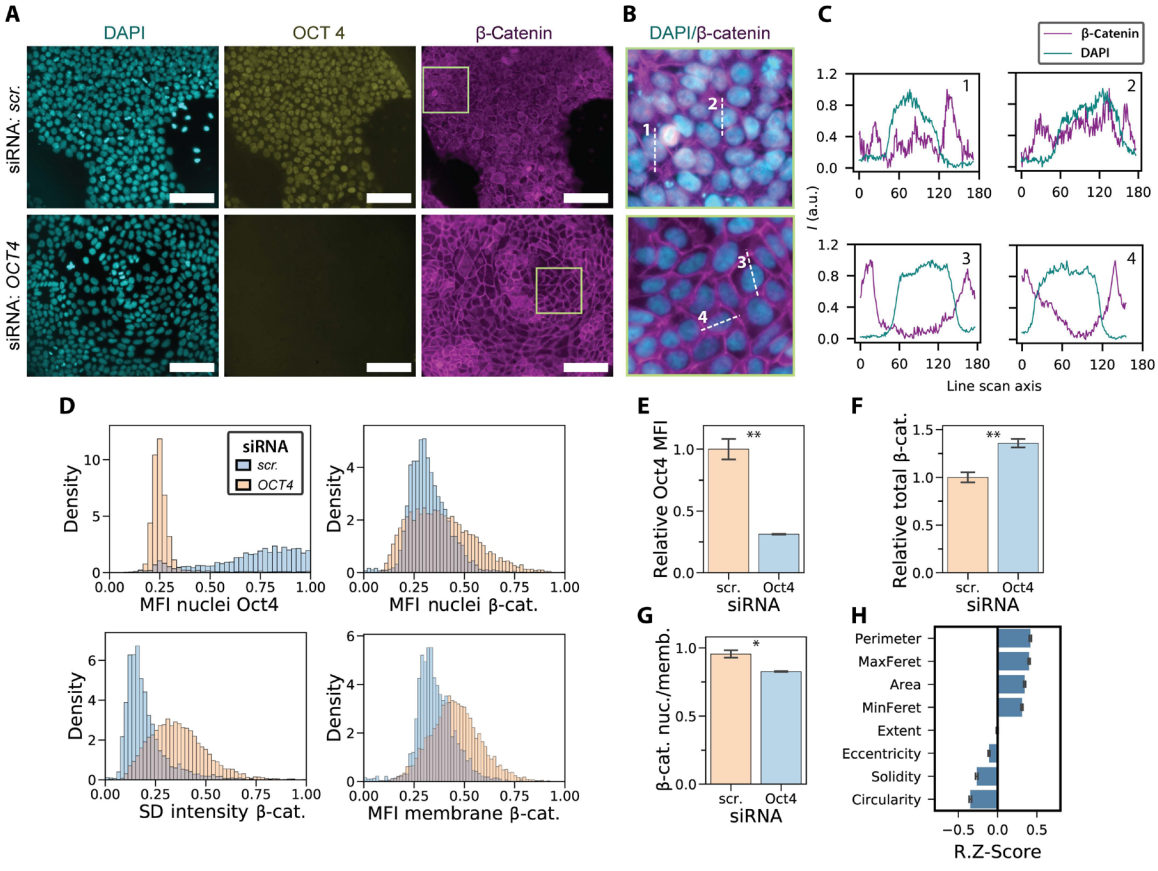

Fig. 7. Delivery of *Oct4* siRNA into hiPSCs. (**A**) Fluorescent micrographs after immunostaining with Oct4 and β-catenin antibodies 72 hours after delivery of scrambled (scr.) and *Oct4*-targeting siRNA. (**B**) Zoomed-in view of cells in the bounding box from (A). (**C**) Line scan of β-catenin across representative cells from (B). (**D**) Top left: Oct4 intensity in the nuclear region. Top right: β-Catenin intensity in the nuclear region. Bottom left: SD of intracellular β-catenin intensity. Bottom right: β-Catenin at the cell membrane. (**E**) Bar plot showing the relative MFI of Oct4 in the siRNA-treated cells. (**F**) Bar plot showing the relative total fluorescence intensity of β-catenin in the siRNA-treated cells. For (E) and (F), data are normalized relative to the scr. case. (**G**) Bar plot showing the ratio of intensity of nuclear to membrane-localized β-catenin. (**H**) Morphology feature comparison between the *Oct4* siRNA– and scr.-treated cells, and all features were standardized using *R.Z.* score with respect to the scr. case. All error bars indicate the SEM of triplicate samples, $n_{cell} > 100$ per sample for all bar plots. $^*P < 0.05$, $^{**}P < 0.01$. Scale bars, 100 μm.

cell and found a statistically significant increase in the total β-catenin expression in cells treated with *Oct4* siRNA relative to the cells treated with the scrambled siRNA (Fig. 7F). This result is consistent with literature reports showing that β-catenin protein levels increase with the down-regulation of *Oct4*, which leads to enhanced Wnt signaling that promotes differentiation (*67*). Previous studies also reveal that translocation of β-catenin from the membrane to the nucleus has been attributed to the WNT signaling pathway (*68*). We quantified the ratio of nuclear intensity to membrane intensity of β-catenin (Fig. 7G) and found the proportion of nuclear β-catenin to be significantly higher in the controls ($P < 0.05$). From our results, we did not observe translocation of β-catenin to the nucleus as a result of the knockdown of Oct4 alone.

Changes in intracellular molecular contents (e.g., RNA and protein levels) are often accompanied by changes in morphology or motility. To characterize the morphology of the cells treated with *Oct4* siRNA relative to controls in our experiments, we measured various shape features for each cell and standardized (*R.Z.* score) each feature using the scrambled siRNA control dataset (Fig. 7H). In this manner, we could compare any changes in shape of the Oct4 knocked-down cells relative to the controls. We observed an increase in the size measurements (e.g., perimeter and area) and a decrease in solidity and circularity for the *Oct4* siRNA–treated cells. In pluripotent stem cells, morphological changes such as enlarged cell size and increased cytoplasmic area have been shown to be a characteristic of cells undergoing differentiation (*69*). Therefore, the morphological changes observed in our study could be due to the hiPSCs being driven away from their ground pluripotent state by the absence of Oct4.

DISCUSSION

In this work, we developed a multiplexed, high-throughput LEPD and combined it with a deep learning–based image analysis pipeline for rapid optimization of experimental conditions required for optimal intracellular delivery and transfection into a wide variety of cell types. We used our LEPD-AI framework to first optimize the device architecture with respect to the electrode geometry by examining the dynamics of calcein extraction from cells due to electroporation under two different electrode geometries and by quantifying the respective resultant changes in cell morphology with the AI-based image analysis pipeline. We observed that cell morphology plays a

key role in efficient localized electroporation, with cells that are likely better adhered to the substrate losing more calcein. This suggests that promotion of adhesion by using extracellular matrix proteins and enhancing cell membrane to substrate contact by centrifugation or fluidic suction should improve the outcome of localized electroporation.

We demonstrated that the multiwell format of the LEPD allows for the tuning of several experimental parameters simultaneously in a single experimental run, thus saving on resources and time. This is especially advantageous for hard-to-transfect cells that might require several iterations to obtain optimized conditions using traditional methods (*8*, *9*). Moreover, the size of the LEPD can be adjusted to make it compatible with different multiwell plate architectures (ranging from 24-well plates to 384-well plates). As a result, different experimental designs are possible depending on whether several conditions need to be tested (small size with larger array) or higher throughput is required for each condition (large size with smaller array). In addition, the transparency and biocompatibility of the LEPD substrate allow for imaging-based assays followed by their analysis using our AI pipeline. This framework can potentially be useful for high-throughput arrayed screening studies (*13*, *70*–*72*), where cells in each LEPD well are transfected with a different cargo (e.g., different siRNAs and Cas9/sgRNA RNPs) to perturb a single gene followed by live-cell tracking (e.g., to study morphology, proliferation, and cell-cell interaction) and end-point high-content imaging (e.g., to look at protein expression) to analyze cell phenotype and identify the top genetic targets.

Using our optimized protocols, we were able to efficiently transfect a wide variety of cell lines and primary/stem cells and found that the LEPD outperformed commercial techniques such as bulk electroporation and Lipofectamine in many cases. Efficient delivery of biomolecular cargo, such as oligonucleotides, siRNA, and plasmid DNA, into a variety of cell types while maintaining high viability in even sensitive cells, such as HDFs and hiPSCs, is especially important for applications involving rare patient-derived cells. Moreover, the versatility is important for a range of cell engineering applications such as biomanufacturing, disease modeling, and developing cell-based therapeutics. Note, however, that the transfection efficiency was lower for the S-HUDEP2 cells compared to the other hard-to-transfect cell types as they are cells in suspension. Future studies with the LEPD can be designed with optimized EP buffers (*37*) and the utilization of additional mechanical stimulation (*34*) to enhance molecular delivery and, consequently, the transfection efficiency in hard-to-transfect suspension cell types. We further demonstrated that the LEPD can deliver multiple cargoes into cells and provide tighter dosage control compared to some traditional methods. This may have potential utility in combinatorial cell perturbation studies where the stoichiometric ratio of the delivered reagents needs to be controlled to affect the biological processes. Specifically, control over dosage could be useful for applications such as iPSC reprogramming where controlling the delivery dosage of transcription factors with precision is necessary. In addition, we demonstrated the capability of the LEPD platform to enable functional gene knockdown in a sensitive and hard-to-transfect cell type (hiPSCs) and performed subsequent analysis of the changes in morphological features and protein expression with single-cell resolution using the AI framework. This demonstrates the potential of the LEPD platform to be used in studies related to stem cell engineering or reprogramming wherein outcomes such as expression levels of multiple proteins, subcellular localization, and morphological changes are important characteristics to be closely monitored.

In summary, we demonstrated that the multiwell format of the LEPD allows for parallel optimization of multiple experimental conditions, specific to a desired application, as well as modular integration with conventional imaging platforms such as fluorescence microscopy for capturing and analyzing data. Overall, the 24-well LEPD offers a compact and flexible cellular delivery and analysis platform that can be tuned toward diverse biological applications that require controlled, high-throughput, multiplexed cell manipulation and analysis.

MATERIALS AND METHODS

Device fabrication

The well plate LEPD PCBs were designed using an electronic automation design software (EAGLE: AutoDesk) and fabricated in a PCB foundry. The bottom PCB plate was bonded to a bottomless 24-well plate using a silicon pressure adhesive (Adhesives Research). Gold-coated electrodes (pins or nail-head stubs) were mounted on the top PCB using push-fit receptacles (MillMax). The LEPD cell culture devices were assembled using sterilized Pyrex glass cloning cylinders bonded to a track-etched PC membrane using silicon pressure adhesive.

Multiphysics simulation

We used COMSOL Multiphysics 5.2a to compute the transmembrane potential in the LEPD system. Simulations were performed using the AC/DC electric currents module. The schematic of the geometry and the details of the material properties and that of the pulse applied are specified in fig. S4 of the Supplementary Materials. The governing equations of the current conservation and boundary condition that were used are

$$\nabla.(\sigma\nabla V)+\nabla.\varepsilon\frac{\partial\nabla V}{\partial t}=0 \quad (1)$$

$$\mathbf{n}.\mathbf{J}=0 \quad (2)$$

where σ is the conductivity (siemens per meter), V is the potential (volts), ε is the permittivity of the relevant domain, $\boldsymbol{n}$ is the surface unit normal vector, and $\boldsymbol{J}$ (ampere per meter squared) is the electric flux vector. The boundary condition of Eq. 2 was used for emulating insulating interfaces in the system, while a nonzero electric potential was applied to the dipped electrode, and ground was applied to the bottom gold electrode (fig. S4). We modeled the cell membrane in Eq. 3 as a thin resistive material with an effective contact impedance

$$\mathbf{n}.\mathbf{J}=\frac{1}{d}\left(\sigma+\varepsilon\frac{\partial}{\partial t}\right)V_m \quad (3)$$

where V_m (volts) is the transmembrane potential and d is the thickness of the cell membrane (meters). A physics-controlled mesh of COMSOL was used to discretize the entire geometry. The simulation was carried out for the entire duration of the pulse, and a backward Euler scheme was used for the time discretization.

Cell culture

Primary HDFs were procured from the American Type Culture Collection (ATCC; PCS-201-012,nd cultured using fibroblast basal medium supplemented with a low-serum growth kit (ATCC, PCS-201-041).

The cells were passaged upon reaching confluency with 0.05% trypsin-EDTA (Life Technologies) and trypsin inhibitor solution. hiPSCs (ATCC, ACS-1019) were cultured in Essential 8 Medium (Thermo Fisher Scientific, A1517001) on Vitronectin (Thermo Fisher Scientific, A14700)–coated six-well plates. Media were replaced every 24 hours. Cells were passaged by dissociating them in 0.5 mM EDTA (Thermo Fisher Scientific) in phosphate-buffered saline (PBS) every 4 to 5 days before reaching full confluency. RevitaCell (100×) (Thermo Fisher Scientific, A2644501) was added at a final concentration of 1× to the media after every passage and transferred to RevitaCell-free media after 24 hours. sHUDEP-2 cells (RIKEN BioResource Center, Tsukuba Branch) were cultured in StemSpan Serum-Free Expansion Medium (STEMCELL Technology) with the following supplements: stem cell factor (50 ng/ml; PeproTech), erythropoietin (20 ng/ml; PeproTech), doxycycline (1 μg/ml; Sigma-Aldrich), 1 μM dexamethasone (Sigma-Aldrich), and penicillin-streptomycin (100 U/ml; Gibco). HeLa (ATCC, CCL-2) and HEK 293T (ATCC, CRL-11268) cells were cultured in DMEM supplemented with 10% fetal bovine serum (FBS) and 1% penicillin-streptomycin. K562 cells (ATCC, CCL-243) were cultured in Iscove's Modified Dulbecco's Medium (Gibco) with 10% FBS (Gibco) (w/v) and 1% penicillin-streptomycin (Gibco).

Cell seeding and culture in LEPDs

The nanoporous polymer membranes of the LEPDs were first coated with appropriate extracellular matrix protein (fibronectin for cell lines and fibroblasts at a concentration of 1 to 5 μg/cm^2; vitronectin for hiPSCs at a concentration of 0.1 to 1 μg/cm^2) and incubated for 1 hour. The devices were left uncoated for cells in suspension. Following this, the devices were washed with PBS twice. For adherent cell types, 5000 to 20,000 cells of interest were pipetted into the LEPD wells in 100 μl of the corresponding culture medium. The cells were then cultured on the polymer surface overnight in an incubator (at 37°C with 5% CO_2) to promote cell adhesion and tight nanopore–cell membrane contact before electroporation the next day. For suspension cells, 15,000 to 40,000 cells were introduced in the LEPDs containing EP buffer and centrifuged at 150*g* for 5 min to establish tight cell contact with the nanopores before electroporation. After electroporation, the LEPD arrays were transferred to 24-well plates (USA Scientific) with the appropriate medium depending on the cell type, in an incubator, and cultured for downstream imaging or assays. All experiments were performed on cultures that were passaged less than 10 times.

General electroporation protocol for delivery and sampling

To deliver the molecular cargo of interest into cells, a 2- to 5-μl droplet of solution containing the cargo at the desired concentration was pipetted at the center of each well of the 24-well plate electroporation system, with each well having a circular (8-mm-diameter) gold-coated bottom electrode. Then, an array of LEPDs with cultured adherent/centrifuged suspension cells in appropriate electroporation media were placed over these cargo droplets. The droplets formed a thin film between the bottom electrode and the nanoporous polymer membrane of the LEPDs having the cells. Last, the lid of the well plate, housing the top gold-coated electrode pins/stubs, was placed over the LEPDs such that these electrodes were in contact with the buffer inside the LEPD chambers, thus forming a closed electrical circuit. A function generator (Agilent) connected to a voltage amplifier (OPA445, Texas Instruments) was used to apply the electroporation pulses [bilevel pulses (V1 = 10 to 50 V; t1 = 0.25 to 1.0 ms; V2 = 10 V; t2 = 0.5 ms to 2.0 ms), 100 to 1000 pulses, 1 to 20 Hz]. Resistance was measured for each LEPD in a well using a multimeter (Agilent) to ensure good electrical connection. The voltage traces were verified on an oscilloscope (Agilent). The pulse application, resistance measurement, and voltage trace verification were controlled from a personal computer using a custom software written in C++.

Bulk electroporation

Bulk electroporation for various primary and stem cell types was carried out using the Gene Pulser XCell System (Bio-Rad) following the manufacturer's protocols. Briefly, 0.2×10^6 to 1×10^6 cells were resuspended in 800 μl of ice-cold media or EP buffer (Bio-Rad). Adherent cell types were dissociated before this step using their respective dissociation reagent (0.05% trypsin with 0.2% EDTA for HDF cells and 0.5 mM EDTA for hiPSCs). The cell suspension was mixed with 20 to 40 μg of the plasmid DNA prepared in TE buffer (1 μg/μl) and introduced into a 0.4-cm prechilled cuvette. The cells were electroporated using recommended electroporation parameters (e.g., 300 V and 500 μF for hiPSCs). The cells were then centrifuged, washed with DPBS, and transferred to well plates (USA Scientific) in their respective prewarmed media. For hiPSCs, the well plates were coated with vitronectin for adhesion, and RevitaCell (Gibco) was added to the media (1× final concentration) to promote viability.

Lipofectamine transfection

Transfection of cell lines using Lipofectamine was carried out following the manufacturer's protocols. Briefly, cells were plated in a 96-well plate and allowed to reach a confluency of 70 to 90% before transfection with LIPO (Thermo Fisher Scientific). For transfecting cells in 1 well of a 96-well plate, 5 μl of Opti-MEM (Thermo Fisher Scientific) was combined with 0.4 μl of LIPO reagent, and 0.1 μg of plasmid (in 5 μl of Opti-MEM) was mixed with 0.2 μl of P3000 reagent. The two solutions were mixed, incubated for 10 min, and then added to the cell culture. Cells were incubated for 48 hours, after which fluorescent protein expression was examined by fluorescence microscopy.

Transfection efficiency and viability assay

For estimating transfection efficiency, the cells were stained with Hoechst 33342 (0.1 mg/ml; Life Technologies) and then imaged using fluorescence microscopy. Values of transfection efficiencies were arrived at by dividing the number of GFP-positive cells by the total number of cells (estimated by Hoechst 33342 staining of nuclei) in the field of view. Cell viability was assayed by live-dead staining with PI 24 hours after intracellular delivery. Briefly, the cells were stained with both PI (Life Technologies) and Hoechst 33342 (Life Technologies) and imaged using fluorescence microscopy. The cells whose nuclei simultaneously expressed PI and Hoechst fluorescence were counted as dead. The viability was therefore calculated using the following expression

$$\text{Viability} = \left(1 - \frac{\text{Cells}_{\text{dead}}}{\text{Cells}_{\text{total}}}\right)$$

DNA oligonucleotide delivery

Thirty-nucleotide-long molecules of DNA oligonucleotide (/5ATTO590N/AC TGG TCA CCT GGT CAT CCT GCC GTA ACT) were purchased from Integrated DNA Technologies and were diluted to 50 μM in 0.1× PBS to serve as the delivery cargo. LEPD-mediated

delivery was done using the localized electroporation protocol described in the "General electroporation protocol for delivery and sampling" section.

siRNA delivery into hiPSCs

POU5F1 (AM16708) and negative control siRNAs (AM4611) were purchased from Thermo Fisher Scientific and diluted to 10 μM in nuclease-free water to serve as the delivery cargo. Cells were seeded into the LEPD wells 24 hours before electroporation, and the siRNAs were delivered using the localized electroporation protocol described in the "General electroporation protocol for delivery and sampling" section.

Immunostaining

All primary and secondary antibodies used were purchased from Thermo Fisher Scientific. The staining protocol specified by the manufacturer-provided manual was followed. Briefly, cells were fixed and permeabilized, and then blocking solution was added. The cells were then incubated with primary antibodies for 3 hours at 4°C. Cells were then washed with the manufacturer-provided washing buffer and incubated with secondary antibodies for another hour. Cells were then washed again, and NucBlue Fixed Cell Stain (DAPI) was added into the last wash step and incubated for 5 min. The primary antibody for both Oct4 (catalog no. A24867) and β-catenin (catalog no. CAT-5H10) was used at a dilution of 1:200. The secondary antibody for Oct4 (catalog no. A24869) was used at a dilution of 1:250, while the secondary antibody for β-catenin (catalog no. A-21235) was diluted 1000 times.

Imaging

Fluorescence images were acquired on a Nikon Eclipse TE 2000 microscope equipped with an Andor Zyla 5.5 sCMOS camera. Image acquisition was controlled using Micro-Manager software. A custom Python script interfacing with Micro-Manager was used to acquire multichannel images from the 24-well plate–format LEPDs. The images of cells after intracellular delivery were acquired with an exposure time of 400 ms under ×4/×10/×20/×40 magnification. For the time-lapse imaging of the calcein depletion experiments, an image was acquired every second with an exposure time of 200 ms using the multidimensional acquisition module of Micro-Manager.

Image processing and segmentation using AI

Raw images were preprocessed using CellProfiler software (*45*) to remove background fluorescence and correct for uneven illumination. An illumination function was calculated from batches of images collected from each experiment and for each fluorescence channel independently.

To identify and segment the cells and their corresponding nuclei in each image, the illuminated-corrected fluorescence images were normalized and passed through an FCN trained to classify each pixel in the image into three corresponding classes (background, interior, and border). The FCN architecture consists of an encoder-decoder scheme containing 20 hidden layers. The encoder portion of the network consists of convolution layers (3 × 3 kernel size) connected with a ReLu activation function and max-pooling layers (2 × 2 kernel size, stride 2) for downsampling. The decoder portion of the network consists of up-convolution layers (2 × 2 kernel size, stride 2) for upsampling and concatenation of upsampled layers with downsampled layers from the encoder portion of the network. To classify each pixel into the three classes, a weighted soft-max loss function was used. The FCN network was trained with fluorescence images and corresponding annotations, labeled with GIMP image manipulation software, with a 5:1 training-to-validation ratio, and optimized using stochastic gradient descent (learning rate: 1×10^{-4}) with momentum. Training was performed on a graphic processing unit (GPU: NVIDIA RTX2080), and the FCN was coded in Python using TensorFlow and Keras packages. The trained FCN model was optimized for inference acceleration (Intel OpenVINO) and integrated into a graphic user interface software coded using C# (Microsoft Visual Studio).

Feature extraction and analysis

The segmented images were passed through a feature extraction pipeline (CellProfiler) to extract various shape and intensity measurements for each individual cell or nucleus in the image. The background intensity was calculated for the surrounding region of each cell by expanding the segmented objects until contacting neighboring objects, and the lower quartile intensity of that local region was subtracted from each cell. The cell and nuclei features were exported in .csv format and analyzed using a custom Python pipeline. The extracted features were glog-transformed (*46*) before *R.Z.* score standardization. The *R.Z.* score standardization procedure was performed for all transformed features for each experiment independently. Following standardization, a Pearson correlation matrix was constructed to measure the correlation across all feature pairs. Highly correlated features above a threshold ($r^2 > 0.9$) were iteratively removed to reduce the number of features for interpretability. A 2D projection of the feature space was obtained using UMAP for dimension reduction to visualize the extracted features.

Statistical analysis

Statistical analysis was performed using Python packages. *P* values were calculated using two-tailed Student's *t* test to determine statistical significance. Two-way ANOVA was used to determine the degree of variability for measurements acquired in different wells of the 24-well LEPD. Normalized data were calculated using max-min normalization.

SUPPLEMENTARY MATERIALS

Supplementary material for this article is available at https://science.org/doi/10.1126/sciadv.abn7637

View/request a protocol for this paper from *Bio-protocol*.

REFERENCES AND NOTES

1. S. M. Prakadan, A. K. Shalek, D. A. Weitz, Scaling by shrinking: Empowering single-cell 'omics' with microfluidic devices. *Nat. Rev. Genet.* **18**, 345–361 (2017).
2. C. Fellmann, B. G. Gowen, P.-C. Lin, J. A. Doudna, J. E. Corn, Cornerstones of CRISPR–Cas in drug discovery and therapy. *Nat. Rev. Drug Discov.* **16**, 89–100 (2017).
3. T. Stuart, R. Satija, Integrative single-cell analysis. *Nat. Rev. Genet.* **20**, 257–272 (2019).
4. M. P. Stewart, A. Sharei, X. Ding, G. Sahay, R. Langer, K. F. Jensen, In vitro and ex vivo strategies for intracellular delivery. *Nature* **538**, 183–192 (2016).
5. M. P. Stewart, R. Langer, K. F. Jensen, Intracellular delivery by membrane disruption: Mechanisms, strategies, and concepts. *Chem. Rev.* **118**, 7409–7531 (2018).
6. N. Oh, J.-H. Park, Endocytosis and exocytosis of nanoparticles in mammalian cells. *Int. J. Nanomedicine* **9** (Suppl. 1), 51–63 (2014).
7. T. Wang, L. M. Larcher, L. Ma, R. N. Veedu, Systematic screening of commonly used commercial transfection reagents towards efficient transfection of single-stranded oligonucleotides. *Molecules* **23**, 2564 (2018).
8. T. L. Roth, C. Puig-Saus, R. Yu, E. Shifrut, J. Carnevale, P. J. Li, J. Hiatt, J. Saco, P. Krystofinski, H. Li, V. Tobin, D. N. Nguyen, M. R. Lee, A. L. Putnam, A. L. Ferris, J. W. Chen, J.-N. Schickel, L. Pellerin, D. Carmody, G. Alkorta-Aranburu, D. del Gaudio, H. Matsumoto, M. Morell, Y. Mao, M. Cho, R. M. Quadros, C. B. Gurumurthy, B. Smith, M. Haugwitz, S. H. Hughes,

J. S. Weissman, K. Schumann, J. H. Esensten, A. P. May, A. Ashworth, G. M. Kupfer, S. A. W. Greeley, R. Bacchetta, E. Meffre, M. G. Roncarolo, N. Romberg, K. C. Herold, A. Ribas, M. D. Leonetti, A. Marson, Reprogramming human T cell function and specificity with non-viral genome targeting. *Nature* **559**, 405–409 (2018).
9. X.-L. Li, G.-H. Li, J. Fu, Y.-W. Fu, L. Zhang, W. Chen, C. Arakaki, J.-P. Zhang, W. Wen, M. Zhao, W. V. Chen, G. D. Botimer, D. Baylink, L. Aranda, H. Choi, R. Bechar, P. Talbot, C.-K. Sun, T. Cheng, X.-B. Zhang, Highly efficient genome editing via CRISPR–Cas9 in human pluripotent stem cells is achieved by transient BCL-XL overexpression. *Nucleic Acids Res.* **46**, 10195–10215 (2018).
10. T. DiTommaso, J. M. Cole, L. Cassereau, J. A. Buggé, J. L. S. Hanson, D. T. Bridgen, B. D. Stokes, S. M. Loughhead, B. A. Beutel, J. B. Gilbert, K. Nussbaum, A. Sorrentino, J. Toggweiler, T. Schmidt, G. Gyuelveszi, H. Bernstein, A. Sharei, Cell engineering with microfluidic squeezing preserves functionality of primary immune cells in vivo. *Proc. Natl. Acad. Sci. U.S.A.* **115**, E10907–E10914 (2018).
11. L. Schmiderer, A. Subramaniam, K. Žemaitis, A. Bäckström, D. Yudovich, S. Soboleva, R. Galeev, C. N. Prinz, J. Larsson, M. Hjort, Efficient and nontoxic biomolecule delivery to primary human hematopoietic stem cells using nanostraws. *Proc. Natl. Acad. Sci. U.S.A.* **117**, 21267–21273 (2020).
12. D. Karra, R. Dahm, Transfection techniques for neuronal cells. *J. Neurosci.* **30**, 6171–6177 (2010).
13. L. Przybyla, L. A. Gilbert, A new era in functional genomics screens. *Nat. Rev. Genet.* **23**, 89–103 (2022).
14. C. E. Thomas, A. Ehrhardt, M. A. Kay, Progress and problems with the use of viral vectors for gene therapy. *Nat. Rev. Genet.* **4**, 346–358 (2003).
15. J. Brooks, G. Minnick, P. Mukherjee, A. Jaberi, L. Chang, H. D. Espinosa, R. Yang, High throughput and highly controllable methods for in vitro intracellular delivery. *Small* **16**, 2004917 (2020).
16. W. Kang, R. L. McNaughton, H. D. Espinosa, Micro- and nanoscale technologies for delivery into adherent cells. *Trends Biotechnol.* **34**, 665–678 (2016).
17. A. Sharei, J. Zoldan, A. Adamo, W. Y. Sim, N. Cho, E. Jackson, S. Mao, S. Schneider, M.-J. Han, A. Lytton-Jean, P. A. Basto, S. Jhunjhunwala, J. Lee, D. A. Heller, J. W. Kang, G. C. Hartoularos, K.-S. Kim, D. G. Anderson, R. Langer, K. F. Jensen, A vector-free microfluidic platform for intracellular delivery. *Proc. Natl. Acad. Sci. U.S.A.* **110**, 2082–2087 (2013).
18. T. Geng, Y. Zhan, J. Wang, C. Lu, Transfection of cells using flow-through electroporation based on constant voltage. *Nat. Protoc.* **6**, 1192–1208 (2011).
19. B. Joo, J. Hur, G.-B. Kim, S. G. Yun, A. J. Chung, Highly efficient transfection of human primary T lymphocytes using droplet-enabled mechanoporation. *ACS Nano* **15**, 12888–12898 (2021).
20. J. Hur, I. Park, K. M. Lim, J. Doh, S.-G. Cho, A. J. Chung, Microfluidic cell stretching for highly effective gene delivery into hard-to-transfect primary cells. *ACS Nano* **14**, 15094–15106 (2020).
21. G. Kang, D. W. Carlson, T. H. Kang, S. Lee, S. J. Haward, I. Choi, A. Q. Shen, A. J. Chung, Intracellular nanomaterial delivery via spiral hydroporation. *ACS Nano* **14**, 3048–3058 (2020).
22. J. Hur, A. J. Chung, Microfluidic and nanofluidic intracellular delivery. *Adv. Sci.* **8**, 2004595 (2021).
23. S. S. P. Nathamgari, N. Pathak, V. Lemaitre, P. Mukherjee, J. J. Muldoon, C.-Y. Peng, T. McGuire, J. N. Leonard, J. A. Kessler, H. D. Espinosa, Nanofountain probe electroporation enables versatile single-cell intracellular delivery and investigation of postpulse electropore dynamics. *Small* **16**, 2002616 (2020).
24. B. Babakinejad, P. Jönsson, A. López Córdoba, P. Actis, P. Novak, Y. Takahashi, A. Shevchuk, U. Anand, P. Anand, A. Drews, A. Ferrer-Montiel, D. Klenerman, Y. E. Korchev, Local delivery of molecules from a nanopipette for quantitative receptor mapping on live cells. *Anal. Chem.* **85**, 9333–9342 (2013).
25. R. Yang, V. Lemaître, C. Huang, A. Haddadi, R. McNaughton, H. D. Espinosa, Monoclonal cell line generation and CRISPR/Cas9 manipulation via single-cell electroporation. *Small* **14**, e1702495 (2018).
26. P. Mukherjee, C. A. Patino, N. Pathak, V. Lemaitre, H. D. Espinosa, Deep learning-assisted automated single cell electroporation platform for effective genetic manipulation of hard-to-transfect cells. *Small* **18**, 2107795 (2022).
27. W. Kang, F. Yavari, M. Minary-Jolandan, J. P. Giraldo-Vela, A. Safi, R. L. McNaughton, V. Parpoil, H. D. Espinosa, Nanofountain probe electroporation (NFP-E) of single cells. *Nano Lett.* **13**, 2448–2457 (2013).
28. O. Guillaume-Gentil, E. Potthoff, D. Ossola, C. M. Franz, T. Zambelli, J. A. Vorholt, Force-controlled manipulation of single cells: From AFM to FluidFM. *Trends Biotechnol.* **32**, 381–388 (2014).
29. Y. Yang, J. Yu, A. Monemian Esfahani, K. Seiffert-Sinha, N. Xi, I. Lee, A. A. Sinha, L. Chen, Z. Sun, R. Yang, L. Dong, Single-cell membrane drug delivery using porous pen nanodeposition. *Nanoscale* **10**, 12704–12712 (2018).
30. P. E. Boukany, A. Morss, W.-c. Liao, B. Henslee, H. Jung, X. Zhang, B. Yu, X. Wang, Y. Wu, L. Li, K. Gao, X. Hu, X. Zhao, O. Hemminger, W. Lu, G. P. Lafyatis, L. J. Lee, Nanochannel electroporation delivers precise amounts of biomolecules into living cells. *Nat. Nanotechnol.* **6**, 747–754 (2011).
31. W. Kang, J. P. Giraldo-Vela, S. S. P. Nathamgari, T. McGuire, R. L. McNaughton, J. A. Kessler, H. D. Espinosa, Microfluidic device for stem cell differentiation and localized electroporation of postmitotic neurons. *Lab Chip* **14**, 4486–4495 (2014).
32. Y. Cao, E. Ma, S. Cestellos-Blanco, B. Zhang, R. Qiu, Y. Su, J. A. Doudna, P. Yang, Nontoxic nanopore electroporation for effective intracellular delivery of biological macromolecules. *Proc. Natl. Acad. Sci. U.S.A.* **116**, 7899–7904 (2019).
33. Y. Cao, H. Chen, R. Qiu, M. Hanna, E. Ma, M. Hjort, A. Zhang, R. S. Lewis, J. C. Wu, N. A. Melosh, Universal intracellular biomolecule delivery with precise dosage control. *Sci. Adv.* **4**, eaat8131 (2018).
34. A. Tay, N. Melosh, Mechanical stimulation after centrifuge-free nano-electroporative transfection is efficient and maintains long-term T cell functionalities. *Small* **17**, 2103198 (2021).
35. H. G. Dixit, R. Starr, M. L. Dundon, P. I. Pairs, X. Yang, Y. Zhang, D. Nampe, C. B. Ballas, H. Tsutsui, S. J. Forman, C. E. Brown, M. P. Rao, Massively-parallelized, deterministic mechanoporation for intracellular delivery. *Nano Lett.* **20**, 860–867 (2020).
36. C. Chiappini, J. O. Martinez, E. De Rosa, C. S. Almeida, E. Tasciotti, M. M. Stevens, Biodegradable nanoneedles for localized delivery of nanoparticles in vivo: Exploring the biointerface. *ACS Nano* **9**, 5500–5509 (2015).
37. P. Mukherjee, S. S. P. Nathamgari, J. A. Kessler, H. D. Espinosa, Combined numerical and experimental investigation of localized electroporation-based cell transfection and sampling. *ACS Nano* **12**, 12118–12128 (2018).
38. Y. Cao, M. Hjort, H. Chen, F. Birey, S. A. Leal-Ortiz, C. M. Han, J. G. Santiago, S. P. Paşca, J. C. Wu, N. A. Melosh, Nondestructive nanostraw intracellular sampling for longitudinal cell monitoring. *Proc. Natl. Acad. Sci. U.S.A.* **114**, E1866–E1874 (2017).
39. P. Mukherjee, E. J. Berns, C. A. Patino, E. Hakim Moully, L. Chang, S. S. P. Nathamgari, J. A. Kessler, M. Mrksich, H. D. Espinosa, Temporal sampling of enzymes from live cells by localized electroporation and quantification of activity by SAMDI mass spectrometry. *Small* **16**, 2000584 (2020).
40. G. He, J. Feng, A. Zhang, L. Zhou, R. Wen, J. Wu, C. Yang, J. Yang, C. Li, D. Chen, J. Wang, N. Hu, X. Xie, Multifunctional branched nanostraw-electroporation platform for intracellular regulation and monitoring of circulating tumor cells. *Nano Lett.* **19**, 7201–7209 (2019).
41. J. Beers, D. R. Gulbranson, N. George, L. I. Siniscalchi, J. Jones, J. A. Thomson, G. Chen, Passaging and colony expansion of human pluripotent stem cells by enzyme-free dissociation in chemically defined culture conditions. *Nat. Protoc.* **7**, 2029–2040 (2012).
42. J. Long, E. Shelhamer, T. Darrell, paper presented at the 2015 IEEE Conference on Computer Vision and Pattern Recognition (CVPR), Boston, MA, 7 to 12 June 2015.
43. C. A. Patino, P. Mukherjee, V. Lemaitre, N. Pathak, H. D. Espinosa, Deep learning and computer vision strategies for automated gene editing with a single-cell electroporation platform. *SLAS Technol.* **26**, 26–36 (2021).
44. T. Falk, D. Mai, R. Bensch, Ö. Çiçek, A. Abdulkadir, Y. Marrakchi, A. Böhm, J. Deubner, Z. Jäckel, K. Seiwald, A. Dovzhenko, O. Tietz, C. Dal Bosco, S. Walsh, D. Saltukoglu, T. L. Tay, M. Prinz, K. Palme, M. Simons, I. Diester, T. Brox, O. Ronneberger, U-Net: Deep learning for cell counting, detection, and morphometry. *Nat. Methods* **16**, 67–70 (2019).
45. A. E. Carpenter, T. R. Jones, M. R. Lamprecht, C. Clarke, I. H. Kang, O. Friman, D. A. Guertin, J. H. Chang, R. A. Lindquist, J. Moffat, CellProfiler: Image analysis software for identifying and quantifying cell phenotypes. *Genome Biol.* **7**, R100 (2006).
46. W. Huber, A. Von Heydebreck, H. Sültmann, A. Poustka, M. Vingron, Variance stabilization applied to microarray data calibration and to the quantification of differential expression. *Bioinformatics* **18**, S96–S104 (2002).
47. J. C. Caicedo, S. Cooper, F. Heigwer, S. Warchal, P. Qiu, C. Molnar, A. S. Vasilevich, J. D. Barry, H. S. Bansal, O. Kraus, M. Wawer, L. Paavolainen, M. D. Herrmann, M. Rohban, J. Hung, H. Hennig, J. Concannon, I. Smith, P. A. Clemons, S. Singh, P. Rees, P. Horvath, R. G. Linington, A. E. Carpenter, Data-analysis strategies for image-based cell profiling. *Nat. Methods* **14**, 849–863 (2017).
48. E. Becht, L. McInnes, J. Healy, C.-A. Dutertre, I. W. Kwok, L. G. Ng, F. Ginhoux, E. W. Newell, Dimensionality reduction for visualizing single-cell data using UMAP. *Nat. Biotechnol.* **37**, 38–44 (2019).
49. C. V. Ly, T. M. Miller, Emerging antisense oligonucleotide and viral therapies for amyotrophic lateral sclerosis. *Curr. Opin. Neurol.* **31**, 648–654 (2018).
50. K. E. Lundin, O. Gissberg, C. I. E. Smith, Oligonucleotide therapies: The past and the present. *Hum. Gene Ther.* **26**, 475–485 (2015).
51. R. B. Ladju, D. Pascut, M. N. Massi, C. Tiribelli, C. H. C. Sukowati, Aptamer: A potential oligonucleotide nanomedicine in the diagnosis and treatment of hepatocellular carcinoma. *Oncotarget* **9**, 2951–2961 (2017).
52. S. Su, B. Hu, J. Shao, B. Shen, J. Du, Y. Du, J. Zhou, L. Yu, L. Zhang, F. Chen, H. Sha, L. Cheng, F. Meng, Z. Zou, X. Huang, B. Liu, CRISPR-Cas9 mediated efficient PD-1 disruption on human primary T cells from cancer patients. *Sci. Rep.* **6**, 20070 (2016).

53. R. Flynn, A. Grundmann, P. Renz, W. Hänseler, W. S. James, S. A. Cowley, M. D. Moore, CRISPR-mediated genotypic and phenotypic correction of a chronic granulomatous disease mutation in human iPS cells. *Exp. Hematol.* **43**, 838–848.e3 (2015).
54. S. H. Park, C. M. Lee, Y. Zhang, A. Chang, V. A. Sheehan, G. Bao, Engineered human umbilical cord derived erythroid progenitor cells (HUDEP2) with sickle or β-thalassemia mutation: An in-vitro system for testing pharmacological induction of fetal hemoglobin. *Blood* **132**, 3478–3478 (2018).
55. C. Wiegand, I. Banerjee, Recent advances in the applications of iPSC technology. *Curr. Opin. Biotech.* **60**, 250–258 (2019).
56. T. E. Ichim, P. O'Heeron, S. Kesari, Fibroblasts as a practical alternative to mesenchymal stem cells. *J. Transl. Med.* **16**, 212 (2018).
57. D. E. Daniels, D. J. Downes, I. Ferrer-Vicens, D. C. J. Ferguson, B. K. Singleton, M. C. Wilson, K. Trakarnsanga, R. Kurita, Y. Nakamura, D. J. Anstee, J. Frayne, Comparing the two leading erythroid lines BEL-A and HUDEP-2. *Haematologica* **105**, e389–e394 (2020).
58. E. P. Papapetrou, M. J. Tomishima, S. M. Chambers, Y. Mica, E. Reed, J. Menon, V. Tabar, Q. Mo, L. Studer, M. Sadelain, Stoichiometric and temporal requirements of Oct4, Sox2, Klf4, and c-Myc expression for efficient human iPSC induction and differentiation. *Proc. Natl. Acad. Sci. U.S.A.* **106**, 12759–12764 (2009).
59. P. Mali, K. M. Esvelt, G. M. Church, Cas9 as a versatile tool for engineering biology. *Nat. Methods* **10**, 957–963 (2013).
60. W. Fujii, K. Kawasaki, K. Sugiura, K. Naito, Efficient generation of large-scale genome-modified mice using gRNA and CAS9 endonuclease. *Nucleic Acids Res.* **41**, e187 (2013).
61. E. J. Aird, K. N. Lovendahl, A. S. Martin, R. S. Harris, W. R. Gordon, Increasing Cas9-mediated homology-directed repair efficiency through covalent tethering of DNA repair template. *Commun. Biol.* **1**, 54 (2018).
62. Ö. Sahin, C. Löbke, U. Korf, H. Appelhans, H. Sültmann, A. Poustka, S. Wiemann, D. Arlt, Combinatorial RNAi for quantitative protein network analysis. *Proc. Natl. Acad. Sci. U.S.A.* **104**, 6579–6584 (2007).
63. P. Zhou, B. K. C. Chan, Y. K. Wan, C. T. L. Yuen, G. C. G. Choi, X. Li, C. S. W. Tong, S. S. W. Zhong, J. Sun, Y. Bao, S. Y. L. Mak, M. Z. Y. Chow, J. V. Khaw, S. Y. Leung, Z. Zheng, L. W. T. Cheung, K. Tan, K. H. Wong, H. Y. E. Chan, A. S. L. Wong, A three-way combinatorial CRISPR screen for analyzing interactions among druggable targets. *Cell Rep.* **32**, 108020 (2020).
64. B. W. Carey, S. Markoulaki, J. H. Hanna, D. A. Faddah, Y. Buganim, J. Kim, K. Ganz, E. J. Steine, J. P. Cassady, M. P. Creyghton, G. G. Welstead, Q. Gao, R. Jaenisch, Reprogramming factor stoichiometry influences the epigenetic state and biological properties of induced pluripotent stem cells. *Cell Stem Cell* **9**, 588–598 (2011).
65. K. Takahashi, S. Yamanaka, Induction of pluripotent stem cells from mouse embryonic and adult fibroblast cultures by defined factors. *Cell* **126**, 663–676 (2006).
66. E. A. Kimbrel, R. Lanza, Current status of pluripotent stem cells: Moving the first therapies to the clinic. *Nat. Rev. Drug Discov.* **14**, 681–692 (2015).
67. M. Abu-Remaileh, A. Gerson, M. Farago, G. Nathan, I. Alkalay, S. Zins Rousso, M. Gur, A. Fainsod, Y. Bergman, Oct-3/4 regulates stem cell identity and cell fate decisions by modulating Wnt/β-catenin signalling. *EMBO J.* **29**, 3236–3248 (2010).
68. J. Massey, Y. Liu, O. Alvarenga, T. Saez, M. Schmerer, A. Warmflash, Synergy with TGFβ ligands switches WNT pathway dynamics from transient to sustained during human pluripotent cell differentiation. *Proc. Natl. Acad. Sci. U.S.A.* **116**, 4989–4998 (2019).
69. Y. Ma, J. Jin, C. Dong, E.-C. Cheng, H. Lin, Y. Huang, C. Qiu, High-efficiency siRNA-based gene knockdown in human embryonic stem cells. *RNA* **16**, 2564–2569 (2010).
70. T. L. Roth, P. J. Li, F. Blaeschke, J. F. Nies, R. Apathy, C. Mowery, R. Yu, M. L. T. Nguyen, Y. Lee, A. Truong, J. Hiatt, D. Wu, D. N. Nguyen, D. Goodman, J. A. Bluestone, C. J. Ye, K. Roybal, E. Shifrut, A. Marson, Pooled knockin targeting for genome engineering of cellular immunotherapies. *Cell* **181**, 728–724.e21 (2020).
71. A. Agrotis, R. Ketteler, A new age in functional genomics using CRISPR/Cas9 in arrayed library screening. *Front. Genet.* **6**, 300 (2015).
72. D. Clymer, S. Kostadinov, J. Catov, L. Skvarca, L. Pantanowitz, J. Cagan, P. LeDuc, Decidual vasculopathy identification in whole slide images using multiresolution hierarchical convolutional neural networks. *Am. J. Pathol.* **190**, 2111–2122 (2020).

Acknowledgments

Funding: Research reported in this publication was supported by the NIH R21 award number 804 1R21GM132709-01 and NIH R01 award number R01HL152314. **Author contributions:** H.D.E. conceived the project and provided overall guidance. C.A.P. designed the multiwell LEPD system. C.A.P., N.P., and P.M. designed and equally contributed to conducting all the biological experiments. C.A.P. and N.P. wrote the custom scripts for image analysis, and C.A.P. developed the AI workflow. N.P. developed and carried out the COMSOL simulations. G.B. and S.H.P. provided the motivation and guidance on experiments with suspended cells. S.H.P. provided the S-HUDEP2 cells and guided the long-term culture of the cells. All authors analyzed the data, discussed the obtained results, and contributed toward writing the manuscript. **Competing interests:** The authors declare that they have no competing interests. **Data and materials availability:** All data needed to evaluate the conclusions in the paper are present in the paper and/or the Supplementary Materials. The S-HUDEP2 cells can be provided by G.B. and S.H.P. pending scientific review and a completed material transfer agreement. Requests for the S-HUDEP2 cells should be submitted to G.B. and S.H.P.

Submitted 17 December 2021
Accepted 7 June 2022
Published 22 July 2022
10.1126/sciadv.abn7637

Science Advances

Multiplexed high-throughput localized electroporation workflow with deep learning–based analysis for cell engineering

Cesar A. PatinoNibir PathakPrithvijit MukherjeeSo Hyun ParkGang BaoHoracio D. Espinosa

Sci. Adv., 8 (29), eabn7637. • DOI: 10.1126/sciadv.abn7637